Mon. Not. R. Astron. Soc. **348,** 333–344 (2004) doi:10.1111/j.1365-2966.2004.07372.x

Substructures in cold dark matter haloes

G. De Lucia,[1]⋆ G. Kauffmann,[1] V. Springel,[1] S. D. M. White,[1] B. Lanzoni,[2] F. Stoehr,[1] G. Tormen[3] and N. Yoshida[4]

[1]*Max-Planck-Institut für Astrophysik, Karl-Schwarzschild-Str. 1, 85748 Garching bei München, Germany*
[2]*INAF-Osservatorio Astronomico di Bologna, via Ranzani 1, 40127 Bologna, Italy*
[3]*Dipartimento di Astronomia, Universita di Padova, vicolo dell'Osservatorio 5, 35122 Padova, Italy*
[4]*Harvard-Smithsonian Center for Astrophysics, 60 Garden Street, Cambridge, MA 02138, USA*

Accepted 2003 November 3. Received 2003 October 31; in original form 2003 June 10

ABSTRACT

We analyse the properties of substructures within dark matter haloes (subhaloes) using a set of high-resolution numerical simulations of the formation of structure in a ΛCDM universe. Our simulation set includes 11 high-resolution simulations of massive clusters as well as a region of mean density, allowing us to study the spatial and mass distribution of substructures down to a mass resolution limit of $10^9\ h^{-1}\ \mathrm{M}_\odot$. We also investigate how the properties of substructures vary as a function of the mass of the 'parent' halo in which they are located. We find that the substructure mass function depends at most weakly on the mass of the parent halo and is well described by a power law. The radial number density profiles of substructures are steeper in low mass haloes than in high-mass haloes. More massive substructures tend to avoid the centres of haloes and are preferentially located in the external regions of their parent haloes. We also study the mass accretion and merging histories of substructures, which we find to be largely independent of environment. We find that a significant fraction of the substructures residing in clusters at the present day were accreted at redshifts $z < 1$. This implies that a significant fraction of present-day 'passive' cluster galaxies were still outside the cluster progenitor and were more active at $z \sim 1$.

Key words: galaxies: clusters: general – galaxies: evolution – galaxies: formation – cosmology: dark matter.

1 INTRODUCTION

The formation and evolution of structure in the Universe is a topic of fundamental interest. In the last few decades, the cold dark matter (CDM) model has been extensively studied and has had considerable success in reproducing observational results, both on galactic and on cluster scales. In fact, the CDM model with the 'concordance' set of cosmological parameters (ΛCDM) has been so successful that it can now be considered a standard paradigm for the formation of structure in the Universe. According to this model, the dominant force that drives structure formation is gravity, and large systems like galaxy clusters are formed via hierarchical merging of smaller structures.

Numerical simulations of gravitational clustering of dark matter are an indispensable tool for investigating the non-linear growth of structures in its full geometrical complexity. Until recently, dissipationless simulations suffered from the so-called *overmerging* problem, i.e. substructures disrupt very quickly within dense environments (Katz & White 1993). However, both analytic work (Moore, Katz & Lake 1996) and high-resolution simulations (Tormen, Bouchet & White 1997; Ghigna et al. 1998; Klypin et al. 1999b; Ghigna et al. 2000) have demonstrated that the cores of dark matter haloes that fall into a cluster can actually survive as self-gravitating objects orbiting in the smooth dark matter background of the cluster, provided high enough force and mass resolution are used. Recent high-resolution simulations (Ghigna et al. 2000; Springel et al. 2001b) have also shown that the abundance of these substructures is in agreement with the observed abundance of galaxies in clusters, suggesting a natural one-to-one identification of luminous cluster galaxies and dark matter substructures.

Another interesting claim is that the shape of the substructure mass function is independent of the mass of the parent halo (Moore et al. 1999b). It is not obvious that this should be the case, because in CDM cosmologies, the initial conditions do depend on scale and galaxies form several billion years before clusters. As Moore et al. (1999b) pointed out, the logarithmic slope of the power spectrum asymptotically approaches −3 on small scales, so clumps of widely different (yet sufficiently small) mass tend to collapse simultaneously, and as a result the time-scale between the collapse of the first substructures and their incorporation into larger haloes becomes shorter. One might therefore expect that substructures were more

⋆E-mail: gdelucia@mpa-garching.mpg.de

easily disrupted in low-mass haloes, producing a substructure mass function which depends on the mass of the parent halo.

Observationally, the predicted abundance of substructures in clusters is one of the major successes of the CDM model (Springel et al. 2001b), but on galactic scales, it appears that simulations predict more substructures than are visible by almost two orders of magnitude (Kauffmann, White & Guiderdoni 1993; Moore et al. 1999a; Klypin et al. 1999b; Tasitsiomi 2002). This is commonly referred to as the 'dwarf galaxy crisis' of CDM. There have been suggestions that the solution to this problem lies in processes such as heating by a photo-ionizing background that suppresses star formation in small haloes at early times (Efstathiou 1992; Bullock, Kravtsov & Weinberg 2000; Benson et al. 2002; Somerville 2002). Alternatively, it has been suggested that the nature of dark matter may be different from that assumed in the canonical ΛCDM model, for example by being *warm* or *self-interacting*, both of which could selectively eliminate small-scale structure. However, self-interactions appear to be relatively ineffective in reducing the number of subhaloes, unless the assumed cross-section is unreasonably large (Colin et al. 2002).

A less drastic resolution was suggested by Stoehr et al. (2002) who noted that it might be possible to identify the observed galactic satellites with the few most massive subhaloes and that the rest contain no stars. Direct evidence for the large population of dark satellites predicted by CDM models comes from the anomalous flux ratios of multiply-imaged quasars (Mao & Schneider 1998; Chiba 2002; Dalal & Kochanek 2002).

So far, a detailed numerical analysis of substructures has only been carried out in high-resolution resimulations of a few individual haloes (Moore et al. 1999b; Ghigna et al. 2000; Springel et al. 2001b). In this paper, we carry out a systematic analysis of substructures as a function of the mass of the parent halo and as a function of environment. We study the mass functions of subhaloes, their radial distributions and their merging and mass accretion histories. These quantities are of fundamental interest for galaxy formation, because dark matter haloes and substructures represent the birth places of luminous galaxies. Their accretion and merging histories regulate the rate at which baryons can cool, determining in this way the rate at which stars form in galaxies as a function of cosmic time.

The layout of the paper is as follows: in Section 2 we describe the simulations that we use; in Section 3 we give a brief description of the algorithm used to find substructures in haloes; in Section 4 we present the subhalo mass function; in Section 5 we analyse the mass distribution of the largest substructures; in Section 6 we study the radial distribution of substructures; and in Section 7 we discuss the merging and mass accretion histories of substructures, both as a function of mass and as a function of environment. A summary and a discussion of the results obtained are presented in Section 8.

2 CLUSTER SIMULATIONS

In this study, we use collisionless simulations of clusters generated using the 'zoom' technique (Katz & White 1993; Tormen et al. 1997). First, a cosmological simulation of a large region is used to select a suitable target cluster. The particles in the final cluster and its surroundings are then traced back to their initial Lagrangian region and are replaced by a larger number of lower-mass particles. These are perturbed using the same fluctuation distribution as in the parent simulation, but now extended to smaller scales to account for the increase in resolution. This resampling of the initial conditions of the Lagrangian region of the cluster thus allows a localized increase in mass and force resolution. Outside the *high-resolution* region, particles of variable mass, increasing with distance, are used so that the computational effort is concentrated on the cluster of interest, while still maintaining a faithful representation of the large-scale density and velocity field of the parent simulation.

Table 1. Numerical parameters for the simulations used. All the simulations were carried out assuming a ΛCDM cosmology with cosmological parameters $\Omega_0 = 0.3$, $\Omega_\Lambda = 0.7$, $\Gamma = 0.21$, $\sigma_8 = 0.9$ and $h = 0.7$. In the table, we give the particle mass m_p in the high-resolution region, the starting redshift z_{start}, the gravitational softening ϵ in the high-resolution region and the number of simulations in each group N.

Name	Description	m_p [h^{-1} M$_\odot$]	z_{start}	ϵ [h^{-1} kpc]	N
B1	10^{15} h^{-1} M$_\odot$clusters	2×10^9	60	5.0	*5*
B2	10^{14} h^{-1} M$_\odot$ clusters	2×10^9	60	5.0	5
S2	10^{15} h^{-1} M$_\odot$ cluster	1.36×10^9	50	3.0	1
M3	field simulation	1.7×10^8	120	1.4	1

In this paper, we study a set of 11 high-resolution resimulations of galaxy clusters (five of mass 10^{14} h^{-1} M$_\odot$ and six of mass 10^{15} h^{-1} M$_\odot$), and a high-resolution resimulation of a 'typical' region of the Universe. The simulations were carried out with the parallel tree-code GADGET (Springel, Yoshida & White 2001).

One of our massive clusters was taken from the 'S-series' studied by Springel et al. (2001b), where the parent simulation employed was the GIF-ΛCDM model carried out by the Virgo Consortium (Kauffmann et al. 1999). This parent simulation followed 256^3 particles of mass 1.4×10^{10} h^{-1} M$_\odot$ within a comoving box of size 141.3 h^{-1} Mpc on a side. The other cluster resimulations and the simulation of the field region were selected from the Very Large Simulation (VLS) carried out by the Virgo Consortium (Jenkins et al. 2001; Yoshida, Sheth & Diaferio 2001). The simulation was performed using a parallel P3M code (Macfarland et al. 1998) and followed 512^3 particles with a particle mass of 7×10^{10} h^{-1} M$_\odot$ in a comoving box of size 479 h^{-1} Mpc on a side. In all cases, the parent simulation and the resimulations were characterized by the following cosmological parameters: $\Omega_0 = 0.3$, $\Omega_\Lambda = 0.7$, spectral shape $\Gamma = 0.21$, $h = 0.7$ (we adopt the convention $H_0 = 100\,h$ km s^{-1}Mpc^{-1}) and normalization $\sigma_8 = 0.9$.

In Table 1, we summarize some important numerical parameters of the simulations used. We will refer to our five high-mass clusters of mass resolution 2×10^9 h^{-1} M$_\odot$ as type 'B1', and to the low-mass clusters as type 'B2'. These simulations were carried out by Barbara Lanzoni as part of her PhD thesis and were previously used in Lanzoni et al. (2003). The 'S2' simulation is taken from the 'S-series' of Springel et al. (2001b). The field region 'M3' was adopted from the 'M-series' studied by Stoehr (2003).

3 IDENTIFICATION OF DARK MATTER SUBSTRUCTURES

The identification of substructures in dark matter haloes is a difficult technical problem and many different algorithms have been developed to accomplish this task, for example the hierarchical friends-of-friends algorithm (HFOF) (Gottlöber, Klypin & Kravtsov 1999), the bound density maximum algorithm (BDM) (Klypin et al. 1999a), and SKID (see http://www-hpcc.astro.washington.edu/tools). Each of these algorithms has its own advantages and weaknesses, so that arguably none of them is completely satisfactory yet. In this work, we use the algorithm SUBFIND proposed by Springel et al. (2001b), which combines ideas used in other group-finding techniques with a topological approach for finding substructure candidates. SUBFIND

can handle haloes of arbitrary shape, does not require an iterative procedure for finding subhalo candidates, and is capable of detecting arbitrary levels of 'subhaloes within subhaloes'. In this section, we briefly summarize how the method works.

In a first step, a standard friends-of-friends (FOF) algorithm is used to identify virialized parent haloes. The FOF algorithm links together all particle pairs with separation less than a linking length b. We adopt the standard value $b = 0.2$ in units of the mean particle separation, which selects groups of particles with overdensities close to the value predicted by the spherical collapse model for the virialized regions of haloes. The next step is to compute an estimate of the local density at the position of each particle in the group. To this end, we employ an adaptive kernel interpolation method similar to the one used in smoothed particle hydrodynamics. In the resulting density field, we define as *substructure candidates* locally overdense regions which are enclosed by isodensity contours that traverse a saddle point. Our method for finding these regions can be visualized as follows: we reconstruct the density field by considering particles in order of decreasing density, thus working our way from high to low density. This corresponds to gradually lowering a global threshold in the density field sampled by the simulation particles. Isolated overdense regions grow slowly in size during this process. When two such separate regions coalesce to form a single region, their density contours join at a saddle point. Each time such an event occurs, we have found two substructure candidates.

After the regions containing substructure candidates have been identified, we apply an unbinding procedure where we iteratively reject all particles with positive total energy in order to eliminate 'background' particles that do not belong to the subhalo. For the purposes of this study, we consider all substructures that survive this unbinding procedure, and still have at least 10 self-bound particles, to be genuine subhaloes.

In summary, the algorithm SUBFIND decomposes a given particle group into a set of disjoint and self-bound substructures, each of which is identified as a locally overdense region in the density field of the background halo. Note that SUBFIND classifies all the particles inside a FOF group either as belonging to a bound substructure or as being unbound. The self-bound part of the FOF background halo itself will then also appear in the substructure list. We will exclude it when referring to subhaloes or substructures in the following analysis.

4 THE SUBHALO MASS FUNCTION

The sample of parent haloes used for studying the mass function analysis consists of 6, 5, 34 and 100 haloes in the mass ranges 8.68×10^{14}–1.79×10^{15} (from simulations B1 and S2), 6.99×10^{13}–1.27×10^{14} (from simulations B2), 7.0×10^{12}–2.0×10^{13} (from simulation M3) and 7.0×10^{11}–2.0×10^{12} h^{-1} $M_\odot$ (from simulation M3).

The resulting subhalo mass functions are shown in Fig. 1. In the first four panels, we plot the differential mass functions for parent haloes of different mass. The histograms are computed by stacking all the haloes in the given range of mass and the error bars represent Poisson errors. The solid line in each of the panels is a power-law fit to the measured differential mass function; the fit is performed using the least absolute deviation method over the range of mass shown by the line. In all the cases the slope of this unrestricted fit is close to -1 (it is equal to -0.98 for the top left panel, -0.97 for the top right panel, -1.11 for the middle left panel and -1.13 for the middle right panel). However, we note that the lowest mass bins, which have the smallest statistical errors, are best fitted with a slightly shallower slope: if we restrict the fit to the four lowest-mass bins the slope is -0.94 for the top left panel and -0.85 for the middle left panel. These are closer to the value -0.8, measured by Helmi, White & Springel (2002) for a single-cluster simulation of extremely high resolution. Also note that a slope shallower than -1 at the low-mass end implies that the integrated mass in substructures remains bounded and is dominated by the most massive subhaloes. It is likely that our subhalo mass functions are steepened somewhat by a cut-off in abundance for very massive substructures.

The bottom left panel of Fig. 1 shows the cumulative mass function for all the haloes used in the sample. To compare the different subhalo mass functions, we have rescaled the subhalo mass by dividing by the virial mass of the parent halo. Each line represents the average cumulative mass function over all the haloes in each mass bin. Note that in this paper we define the 'virial mass' as M_{200}, the mass within a sphere of density 200 times the critical value at redshift zero. The lines end at different places because of the differing mass resolution of the simulations (see Table 1). We find that all four cumulative mass functions agree within the statistical errors. Finally, in the bottom right panel, we show the differential subhalo mass functions in units of rescaled mass.

We note that the 'universality' of the subhalo mass function seen here appears to be quite robust with respect to numerical resolution. In Fig. 2 we compare the average cumulative mass functions for haloes with mass $\simeq 10^{14}\,h^{-1}\,M_\odot$ from simulations B2 and M3. We here averaged five haloes for simulations B2, and four for simulation M3, to reduce the object-to-object scatter that is unavoidable for small numbers of subhaloes. Despite an order-of-magnitude difference in numerical resolution, the agreement between the simulations is good. We are able to resolve the right number of objects in the low-resolution simulation above its resolution limit (shown as a vertical dotted line in the figure). A similar result was obtained by (Springel et al. 2001b see their fig. 5) using a set of four resimulations of the same cluster with systematically increasing resolution, thereby allowing a direct study of numerical convergence. This showed in particular that the S2 simulation used here has well converged to the properties of a much higher-resolution simulation above its own resolution limit, as used here. Further support for our results was also found by Stoehr et al. (2003, see their fig. 3). They compared the S-series simulations from Springel et al. (2001b) with an extremely well-resolved resimulation of a Milky-Way-sized halo. This latter simulation used an updated version of the simulation code and more conservative integration parameters than used here (following Power et al. 2003), suggesting that the subhalo mass function is a relatively robust quantity and that the simulations we discuss here are adequate for our purposes.

As a further check of the robustness of our results we also compare the internal structure of subhaloes drawn from our different simulations. Fig. 3 shows the correlation between the substructure mass and the third power of the maximum circular velocity, $V_{\rm max}$, measured directly from the circular velocity curve of each subhalo. Different symbols are used for substructures drawn from different simulations. Note that for the range of masses shown in the plot, substructures drawn from simulation M3 contain at least 60 particles. While the scatter is clearly large for haloes with such a low number of particles, the good general agreement between the runs suggests that the smallest substructures in our lower-resolution simulations have an internal structure that is still reliably resolved, at least in a statistical fashion.

Our results confirm the conclusion drawn by Moore et al. (1999b): the mass function of substructures appears to be almost independent of the mass of the parent halo. While our results are consistent with

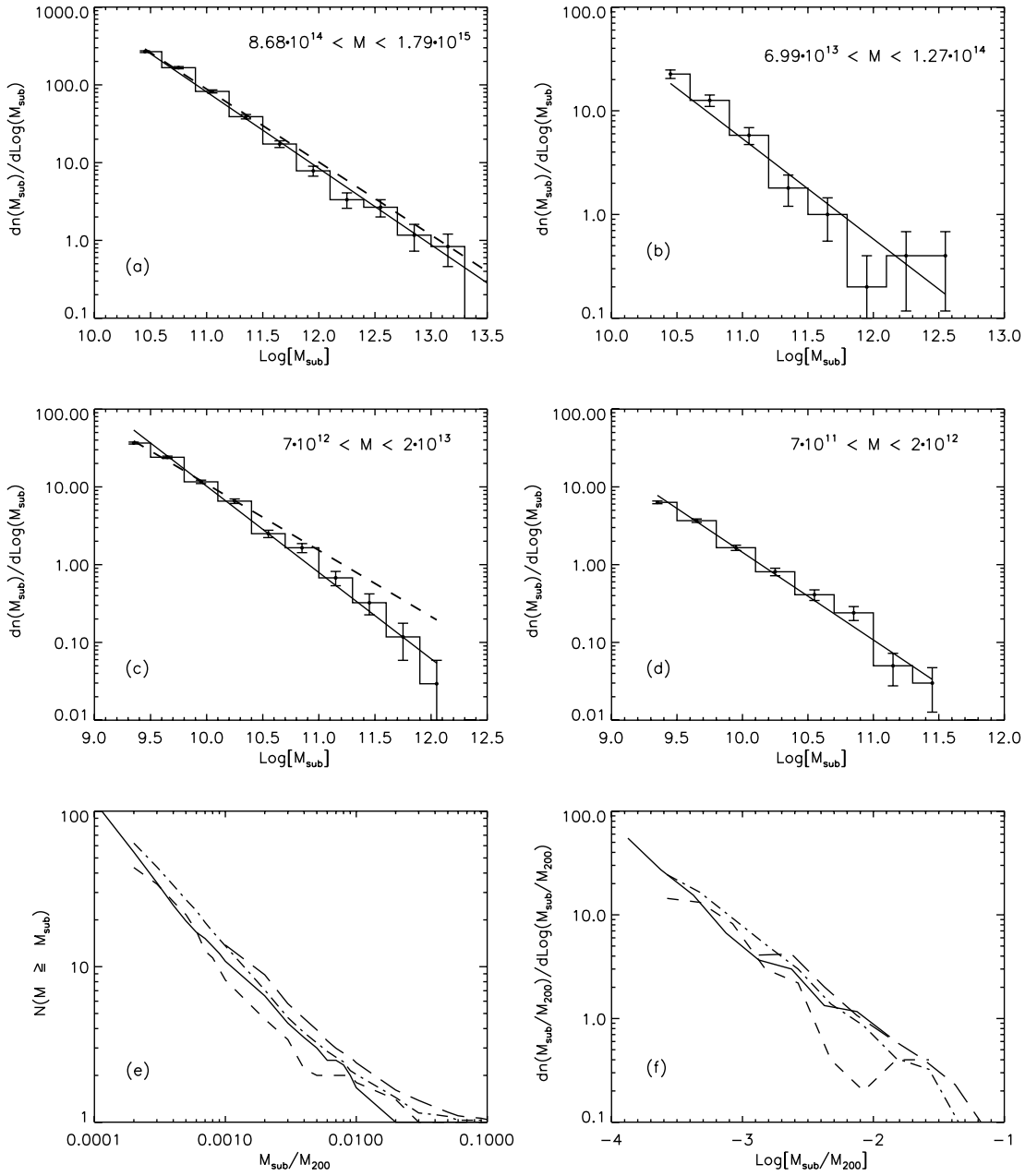

Figure 1. Panel (a)–(d): the differential mass function of subhaloes residing in parent haloes of different mass. The solid line represents a power law fit to the mass function. The dashed line shown in panels (a) and (c) represents a fit restricted to the four lowest-mass bins. The masses are in units of $h^{-1}\,\mathrm{M}_{\odot}$. The range of mass of the haloes used in each bin is indicated in each panel. Panel (e): the cumulative mass function of subhaloes in units of rescaled subhalo mass. The solid line is for haloes with mass $\simeq 10^{15}\,h^{-1}\,\mathrm{M}_{\odot}$, the dashed line is for haloes with mass $\simeq 10^{14}\,h^{-1}\,\mathrm{M}_{\odot}$, the dash-dotted line is for haloes with mass $\simeq 10^{13}\,h^{-1}\,\mathrm{M}_{\odot}$, and the long-dashed line is for haloes with mass $\simeq 10^{12}\,h^{-1}\,\mathrm{M}_{\odot}$. Panel (f): differential mass functions in units of rescaled subhalo mass; the different line styles are the same as in panel (e).

such a 'scale-free' subhalo mass function, the halo-to-halo scatter in our simulation set is quite large, preventing us from putting tight constraints on the accuracy with which the 'scale-free' subhalo mass function is preserved when haloes of different mass are considered, and hence there is still room for weak trends with mass. A clear detection of these would require simulations with larger dynamic range, and larger samples of simulated haloes for each mass bin.

As we discuss in more detail in Section 7.2, our findings suggest that the destruction of satellites due to the physical processes of dynamical friction and tidal stripping on one hand, and the accretion of new satellites on the other hand, cancel out in such a way that the subhalo mass function does not depend or at best very weakly depends on the mass of the parent halo. The reason for the invariance of the subhalo mass function may lie in the physical nature of this dynamical balance, which may be insensitive to the slightly broken scale invariance of dark haloes themselves. This shows up as a mass-dependence of halo concentrations, for example. Some fully analytic models for the subhalo abundance have been developed (e.g. Sheth 2003), but they are presently not able to account for mass-loss and dynamical friction self-consistently, and so provide little guidance to

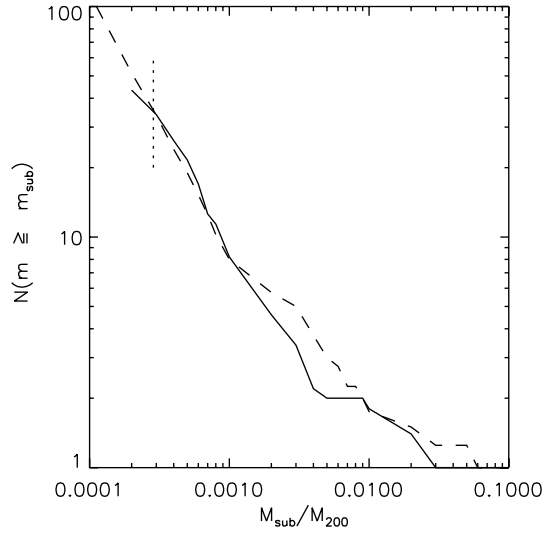

Figure 2. The cumulative mass function of subhaloes in units of rescaled subhalo mass for haloes with mass $\simeq 10^{14}\ h^{-1}\ \mathrm{M}_{\odot}$. The solid line corresponds to the average of haloes from simulations B2 and the dashed line to haloes from simulation M3. The vertical dotted line shows the resolution limit corresponding to simulations B2.

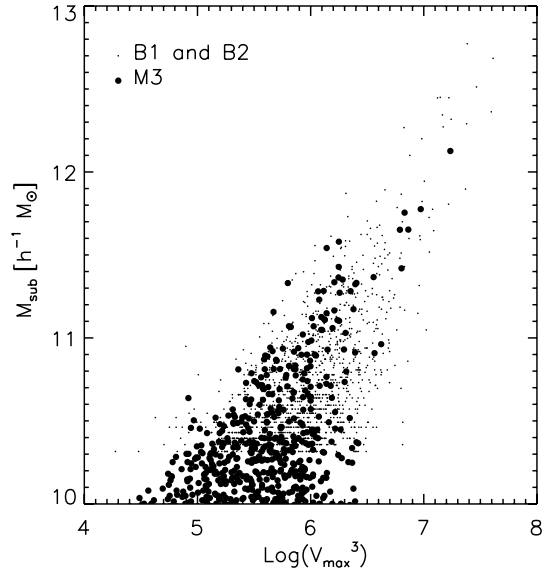

Figure 3. Substructure masses as a function of V_{max}^3 for subhaloes drawn from our different simulations. Small dots are used for subhaloes that reside in haloes with mass $\sim 10^{15}\ h^{-1}\ \mathrm{M}_{\odot}$ (from simulations B1) and $\sim 10^{14}\ h^{-1}\ \mathrm{M}_{\odot}$ (simulations B2) and filled circles for subhaloes in haloes with mass $\sim 10^{13}\ h^{-1}\ \mathrm{M}_{\odot}$ (simulation M3). V_{max} was determined as the maximum of the circular velocity curve of each subhalo.

answer this interesting question. A full understanding of the apparent 'conspiracy' that establishes an almost mass-invariant subhalo mass function will therefore require further simulations.

5 THE MOST MASSIVE SUBSTRUCTURES

In this section we investigate whether the properties of the largest substructures depend on the mass of the parent halo. This is interesting since the largest substructures mark the sites where one expects to find the brightest galaxies.

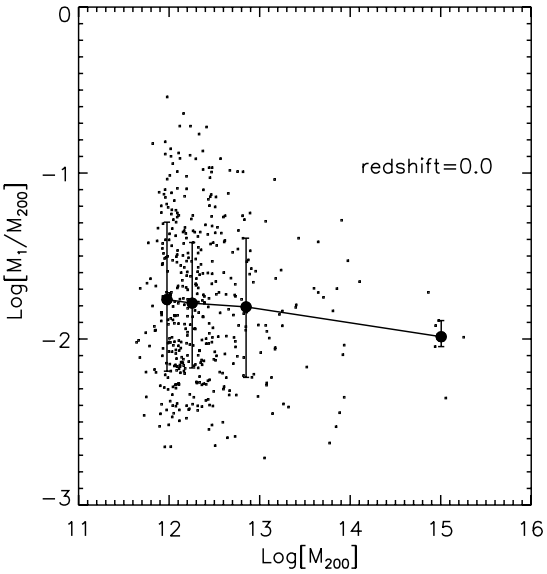

Figure 4. Ratio of the mass of the most massive substructure and the parent halo mass as a function of parent halo mass. The small symbols represent the values measured for each individual halo; the filled circles are the median in bins of halo mass chosen so that each of them contains the same number of points (143). The last six points, corresponding to the main haloes of simulations B1 and S2, are treated as a separate bin. The error bars mark the 20th and 80th percentiles of the distribution.

In the following, M_1 refers to the mass of the most massive subhalo and M_2 to the mass of the second most massive subhalo within the virial radius of a given object of virial mass M_{200}. Note that we have excluded from our analysis the subhalo associated with the FOF group itself. In a semi-analytic scheme, it is this 'subhalo' that would host the brightest cluster galaxy (BCG). In Section 7.2 we will show that, once accreted on to a massive halo, substructures suffer significant stripping, an effect that is more important for substructures accreted at higher redshift. It is then likely that the largest substructures we find within the virial radius at the present time were accreted at relatively low redshift.

In Fig. 4, we plot M_1/M_{200} as a function of M_{200} for 434 haloes drawn from all the simulations listed in Table 1. This sample includes not only the central clusters in our resimulations, but also the other haloes found in the high-resolution regions around the resimulated objects down to a mass limit of $10^{13}\ h^{-1}\ \mathrm{M}_{\odot}$. We took care however to exclude *contaminated* haloes that contained low-resolution particles. In simulation M3, we selected only haloes with a mass larger than $10^{12}\ h^{-1}\ \mathrm{M}_{\odot}$. The small symbols in Fig. 4 indicate the value of M_1/M_{200} measured for each individual halo, while the filled circles represent the median of the distribution. We have taken bins in M_{200} such that there is an equal number (143) of haloes in each bin, except for the last six points, which we treated as a separate bin, corresponding to the central cluster haloes in simulations B1 and S2. The error bars mark the 20th and 80th percentiles of the distribution.

The results in Fig. 4 suggest that M_1/M_{200} depends very little on the mass of the parent halo. Interestingly, M_1/M_{200} appears to exhibit less scatter for the most massive haloes, but the number of simulated clusters we have in this high-mass regime is rather small, so it is unclear whether this effect is statistically significant.

The results in Fig. 4 imply that the median value of M_1 increases in proportion to the mass of the cluster, suggesting that second-ranked

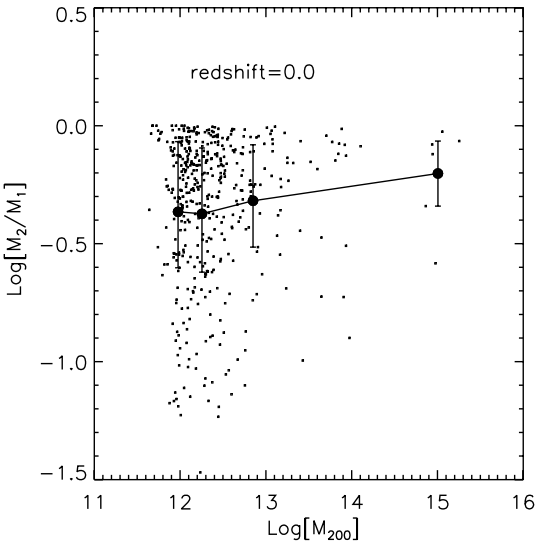

Figure 5. Ratio in mass between the two most massive substructures as a function of the parent halo mass. As in Fig. 4, small symbols represent the values measured for each individual halo, while the filled circles give the median in the same bins as in Fig. 4. The error bars mark the 20th and 80th percentiles of the distribution.

galaxies will be more luminous in more massive haloes. Note also that the mass of the largest substructure within the virial radius is typically only a few per cent of the virial mass.

In Fig. 5, we show the ratio M_2/M_1 as a function of the mass of the parent halo. Once again there is rather little dependence on M_{200} with a possible decrease in the scatter for more massive haloes. Note that the median value of M_2/M_1 is around 0.5. If the stellar masses of the second- and third-brightest galaxies in a cluster scale simply with the masses of their dark subhaloes, they should have K-band luminosities that are equal to within 0.5 mag.

6 THE RADIAL DISTRIBUTION OF SUBHALOES

The large sample of subhaloes in our simulations allows us to study their radial distribution and to investigate how it depends on the mass of the parent halo. In Fig. 6, we plot the number density of substructures as a function of the normalized distance R/R_{200} from the centre of the halo, defined here as the position of the most bound particle in the halo. We show averaged results for haloes with masses $\sim 10^{15}\ h^{-1}\ \mathrm{M}_\odot$, $\sim 10^{14}\ h^{-1}\ \mathrm{M}_\odot$, and $\sim 10^{13}\ h^{-1}\ \mathrm{M}_\odot$, and we limit the analysis to subhaloes with masses greater than a fixed fraction (2×10^{-4}) of the virial mass of the parent halo. This fraction is chosen because it lies just above the mass limit where it is possible to identify substructures in all of our simulations. As Fig. 1 shows, there are typically ~ 50 subhaloes per parent halo with $M_{\rm sub}/M_{200} > 2 \times 10^{-4}$, so by stacking a large sample of haloes, it is possible to calculate an average density profile that has rather little noise. Note that the densities plotted in Fig. 6 have been normalized to the mean density inside the virial radius. The solid lines with symbols show results for the three different parent halo mass ranges defined above. For comparison, we have also plotted the dark matter radial profiles as dashed lines. Note that a small shift in the abscissa has been added to make the plot more readable.

We find that the subhalo profiles are 'antibiased' relative to the dark matter in the inner regions of the haloes. This agrees with the

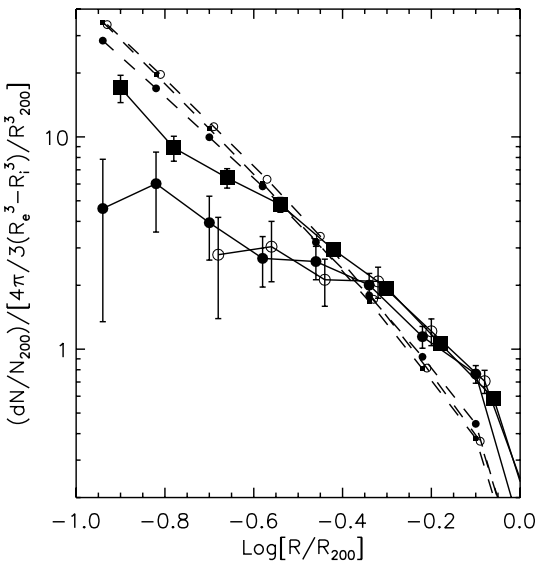

Figure 6. Radial distribution of substructures in haloes of different mass. Lengths are given in units of R_{200} and densities are normalized to the mean density inside R_{200}. Symbols connected by solid lines show the number density profile of substructures (filled circles are for $10^{15}\ h^{-1}\ \mathrm{M}_\odot$ haloes, empty circles for $10^{14}\ h^{-1}\ \mathrm{M}_\odot$ haloes and filled squares for $10^{13}\ h^{-1}\ \mathrm{M}_\odot$ haloes). Symbols connected by dashed lines show the corresponding dark matter profiles.

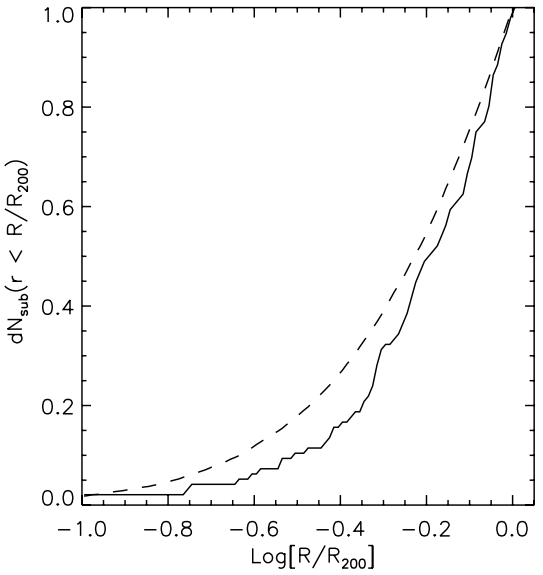

Figure 7. Cumulative radial distribution of the number of substructures in two different mass ranges in the simulation M3. The dashed line is for substructures with $M_{\rm sub} < 0.01\ M_{200}$, and the solid line is for $M_{\rm sub} > 0.01\ M_{200}$.

results of Ghigna et al. (2000). Surprisingly we also find that the radial number density profiles are steeper in low-mass haloes than in high-mass haloes, a finding that deserves further investigation.

We now use our highest-resolution cluster simulation to investigate whether subhaloes of different mass have different radial profiles. In Fig. 7, we show the cumulative fraction of substructures as a function of R/R_{200} for subhaloes with $M_{\rm sub} > 0.01\ M_{200}$ (solid line) and $M_{\rm sub} \leqslant 0.01\ M_{200}$ (dashed line).

As Fig. 1 already made clear, there are many more substructures with $M_{\rm sub} \leqslant 0.01\,M_{200}$ than with $M_{\rm sub} > 0.01\,M_{200}$ (9749 versus 96). Fig. 7 now shows that more massive substructures are preferentially located in the external regions of their parent haloes. This can be understood as a consequence of tidal truncation and stripping effects that quickly decrease the mass of subhaloes as they fall into the cluster and reach the dense inner cores of the parent haloes (see Section 7.2 for a more quantitative analysis of mass-loss due to stripping).

Also note that this finding can be naturally explained as a consequence of the orbital decay experienced by substructures. As shown in Tormen, Diaferio & Syer (1998), the orbital decay is consistent with expectations based on the combined effects of dynamical friction and mass loss. As a result, massive substructures are driven to the centre more rapidly than less-massive ones: Tormen et al. show that the orbital decay occurs in less than a Hubble time if the initial mass of substructures is larger than 1 per cent of the mass of the main cluster, while the substructures can retain their identity for a significant fraction of the Hubble time if their mass is smaller than 5 per cent of the main cluster mass. Once driven to the centre, massive substructures are destroyed and are no longer distinguishable from the central halo; this naturally explains the mass segregation that we see in our simulations.

In Fig. 8, we show the cumulative fraction of the total mass of the parent halo that is in substructures as a function of normalized distance from the halo centre. The different lines and symbols have the same meaning as in Fig. 6 and represent median relations for all the haloes in each mass bin. The error bars mark the 20th and 80th percentiles of the distribution. The mass fraction in substructures rises from $\simeq 1$ per cent at a radius $\simeq 0.3\,R_{200}$ to $\sim$6 per cent at $r \sim R_{200}$. Note that the total mass fraction is dominated by the small number of most massive subhaloes, and is hence a rather noisy quantity that shows large variations from system to system. The mass fraction may also reach values above $\simeq$ 10–15 per cent, but

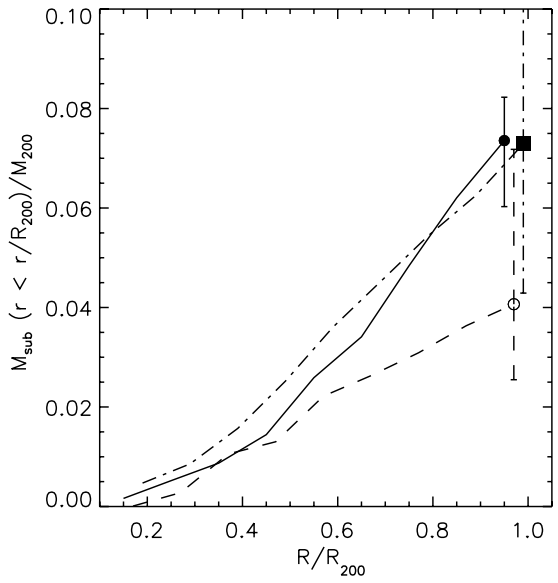

Figure 8. Cumulative mass fraction in substructures as a function of the distance from the halo centre for haloes of different mass. The solid line is for haloes of mass $\simeq 10^{15}\,h^{-1}\,{\rm M}_\odot$, the dashed line for haloes of mass $\simeq 10^{14}\,h^{-1}\,{\rm M}_\odot$, and the dash-dotted line for haloes of mass $\simeq 10^{13}\,h^{-1}\,{\rm M}_\odot$. The error bars on the last point mark the 20th and 80th percentiles of the distribution.

then the underlying FOF parent halo is typically quite aspherical, with the most massive subhalo often lying outside the formal radius R_{200} of the parent halo.

7 SUBHALO HISTORIES

So far we have analysed the properties of subhaloes only at redshift $z = 0$. In this section, we turn to the time evolution of the masses of subhaloes and their merging histories.

In order to carry out this analysis, we have measured *merger trees* for each subhalo from the simulations. These trees allow us to specify all the progenitors (or the descendants) of a substructure at each epoch. To build the merger trees, we use a slightly modified version of the code described in Springel et al. (2001b). We briefly review the main features of the relevant algorithms in the following section.

7.1 Constructing merging trees

Following Springel et al. (2001b) we define a subhalo $S_{\rm B}$ at redshift $z_{\rm B}$ to be the *progenitor* of a subhalo $S_{\rm A}$ at redshift $z_{\rm A}$ (with $z_{\rm A} < z_{\rm B}$) if more than one-half of the $N_{\rm link}$ most bound particles belonging to $S_{\rm B}$ end up in $S_{\rm A}$. Springel et al. (2001b) adopted $N_{\rm link} = 10$. However, we obtained considerably better results with a value of $N_{\rm link}$ that varies between 10 for the less-massive substructures to 100 for more massive ones. In this way, occasional failures of the code when building the merger trees were more robustly avoided. Particularly if substructures undergo major mergers, the code identified in some cases the wrong progenitor for $N_{\rm link} = 10$, or lost track of an entire subhalo. We have also updated the code so that volatile links to 'evanescent' substructures (i.e. objects close to the resolution limit that occasionally appear and then disappear) are avoided.

With these choices, we manage to trace 85–90 per cent of all the substructures in our simulations back to the point when they were first accreted. This fraction goes up to 87–93 per cent if we only consider substructures with more than 100 particles.

7.2 Mass accretion history

We now use our merging trees to study the *mass accretion histories* of the subhaloes in our simulations. Van den Bosch (2002) has carried out a similar analysis for dark matter haloes and has proposed an analytic expression for the mass accretion function based on the extended Press–Schechter formalism (Press & Schechter 1974; Bond et al. 1991; Bower 1991). This function was found to be in excellent agreement with the results of high-resolution N-body simulations. Our aim is to study the mass accretion function for subhaloes and study whether there is any dependence on mass or on environment.

We have selected subhaloes at redshift $z = 0$ in two different mass ranges ($\simeq 10^{11}\,h^{-1}\,{\rm M}_\odot$ and $\simeq 10^{12}\,h^{-1}\,{\rm M}_\odot$). In order to test for the effects of environment, we selected on one hand subhaloes that reside within the virial radius of the massive clusters that formed in simulations B1 and B2 by the present day, and on the other hand subhaloes located within the smaller haloes found in simulation M3. In the following, we will refer to the substructures in the clusters as *cluster subhaloes* and to the substructures inside the smaller haloes of M3 as *field subhaloes*. Note that since we have excluded from our analysis the main subhalo associated with the FOF group and since on average the most massive substructure has a mass a few per cent of M_{200} (see Fig. 4) we end up with very few substructures selected from M3. In particular we have only five substructures with a mass $\sim 10^{12}\,h^{-1}\,{\rm M}_\odot$ and 38 substructures with a mass

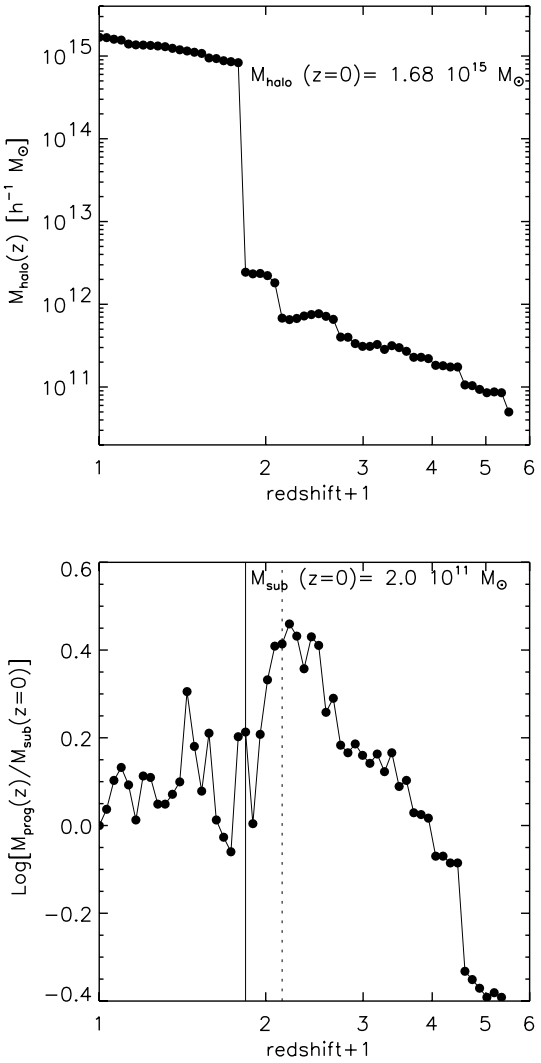

Figure 9. Example for a typical mass accretion history for a subhalo of mass $2 \times 10^{11}\ h^{-1}\ \mathrm{M}_\odot$ (lower panel), and the corresponding variation of mass for the parent halo in which the subhalo resides (top panel). The vertical solid line corresponds to the last time the subhalo is outside the main progenitor of the cluster; the dotted line corresponds to the time the subhalo becomes a substructure (see the text for details).

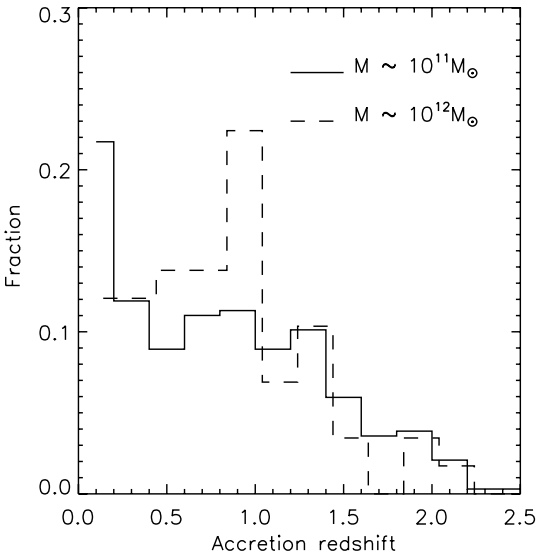

Figure 10. Distribution of the accretion redshifts for the cluster subhalo sample. A small shift is added to the abscissa to produce a more readable plot.

$\sim 10^{11}\ h^{-1}\ \mathrm{M}_\odot$. The corresponding numbers for the substructures selected from simulations B1 and B2 are 62 and 338.

For each of these samples, we build the mass accretion histories as follows: we start from a particular subhalo at redshift $z = 0$ and construct its merger tree as described in the previous section. At each redshift we track the history of the selected subhalo by linking it with its most massive progenitor.

In Fig. 9 we show a typical example of a mass accretion history for a subhalo with mass $2 \times 10^{11}\ h^{-1}\ \mathrm{M}_\odot$ at redshift zero. In the lower panel, we show the mass accretion history of the subhalo and in the upper panel, the corresponding mass of the halo in which the subhalo resides at each redshift.

In this example, the subhalo was accreted on to a larger halo at redshift ~ 1 (shown as a dotted line on the plot). For times prior to this event the substructure was a main subhalo, i.e. the subhalo corresponding to a FOF group, and its mass grew monotonically in time. From now on, we will refer to this event as the *accretion time* ($t_{\rm accr}$) of the subhalo. A few snapshots later, at redshift ~ 0.8, the substructure and its host halo were accreted on to the main progenitor of the cluster (shown as a solid line on the plot).

After the subhalo is accreted, it suffers significant tidal stripping and *decreases* in mass. In this particular example, the final mass of the subhalo is $\simeq 40$ per cent of the value at its accretion time.

We find that for ~ 60 per cent of the subhaloes in the 10^{11} mass bin and ~ 80 per cent of the subhaloes in the 10^{12} bin the accretion event corresponds to the accretion of the substructure on to the main progenitor of the cluster itself. For most of the rest, the time elapsed between these two events is fairly short. The results we will show later are essentially unchanged if we adopt as the definition of the accretion time, the accretion of the substructure on to the main progenitor of the cluster itself.

Fig. 10 shows the distribution of the accretion redshifts for the cluster substructures in our sample. Interestingly, we find that a large fraction of the substructures is accreted at redshift $z < 1$. As noted above, for most of these substructures this accretion event corresponds to the accretion on to the main cluster itself. Our results hint that substructures are constantly erased in the cluster, being replenished by newly infalling haloes.

In Fig. 11, we plot the distribution of $M(t = t_0)/M(t = t_{\rm accr})$, i.e. the ratio of the mass of the subhalo at the present day to the mass it had when it was first accreted. The histograms show that this ratio has a quite broad distribution, varying from a value of ~ 1 to ~ 0.1. We note that most of the subhaloes that have lost only small amounts of mass have been accreted very recently.

This is more clearly shown in Fig. 12 where we plot the average mass accretion function for the cluster subhaloes in the two mass bins considered. Three different accretion redshift intervals are considered and in all cases the subhalo masses are normalized to the mass of the subhalo at $t_{\rm accr}$. The thick solid line shows the mean relation for subhaloes with mass $\sim 10^{11}\ h^{-1}\ \mathrm{M}_\odot$, while the thin line shows the relation for $M_{\rm sub} \sim 10^{12}\ h^{-1}\ \mathrm{M}_\odot$. The mass accretion function monotonically increases for times prior to the accretion event. Once the substructures are accreted, tidal stripping is effective and operates on short time-scales. The longer the substructure spends in a more massive halo, the larger is the destructive effect of tidal stripping. Substructures remaining at $z = 0$ that were accreted

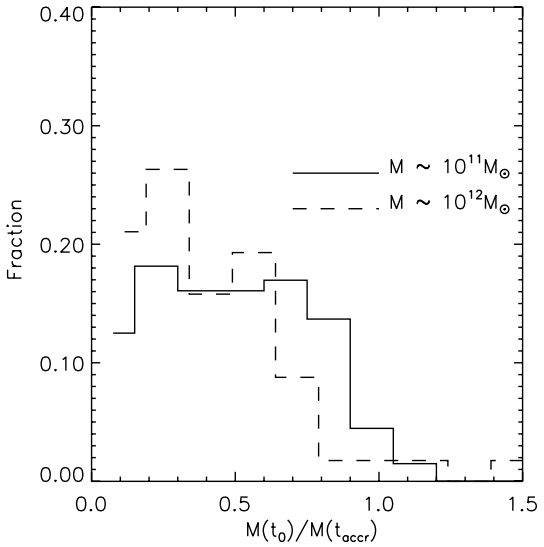

Figure 11. Distribution of the quantity $M(t = t_0)/M(t = t_{\rm accr})$ for the cluster subhalo sample. A small shift is added to the abscissa to produce a more readable plot.

at redshift larger than 1 (panel c) have been typically stripped of ∼80 per cent of their mass. There is also a slight indication that stripping is more effective for more massive substructures: panels (a) and (b) show that more massive substructures have been stripped significantly more than less massive substructures accreted at the same redshift. This effect does not appear in panel (c) but note that we have very few objects accreted in this redshift bin in our sample of more massive subhaloes.

In Fig. 13 we compare the mass accretion histories of field and cluster subhaloes. We limit the analysis to substructures with mass $\sim 10^{11}\ h^{-1}\ {\rm M}_\odot$. Again the mass accretion function is normalized to the mass of the subhalo at the accretion time. We find that field subhaloes and cluster subhaloes have remarkably similar histories suggesting that the efficiency of the tidal stripping is largely independent of the mass of the parent halo.

7.3 Merging histories

In hierarchical models of galaxy formation, galaxies and their associated dark matter haloes form hierarchically through merger and accretion processes. In this context, the term *merger* is usually used to refer to an interaction between two objects of similar mass, while the term *accretion* is used to describe the infall of small objects on to much more massive haloes.

Observational results and numerical simulations confirm that interactions (such as tidal truncation or collisions) play an important role in the evolution of galaxies. There is, for example, solid evidence (Schweizer & Seitzer 1992; Whitmore et al. 1997; Barnes 1999) that at least some elliptical galaxies are the result of mergers between disc galaxies of similar mass. Mergers may also have a strong effect on the baryonic component of galaxies; they can trigger bar-instabilities in stellar discs and cause an inflow of gas into the centres of galaxies, fuelling AGN activity or starbursts.

Following the merger tree of the substructures in our sample we can analyse in detail the merger history, distinguishing between mergers and accretion events. To build the merger history we proceed as follows: we consider all the substructures within the virial radius at redshift zero and follow their merger trees back in time,

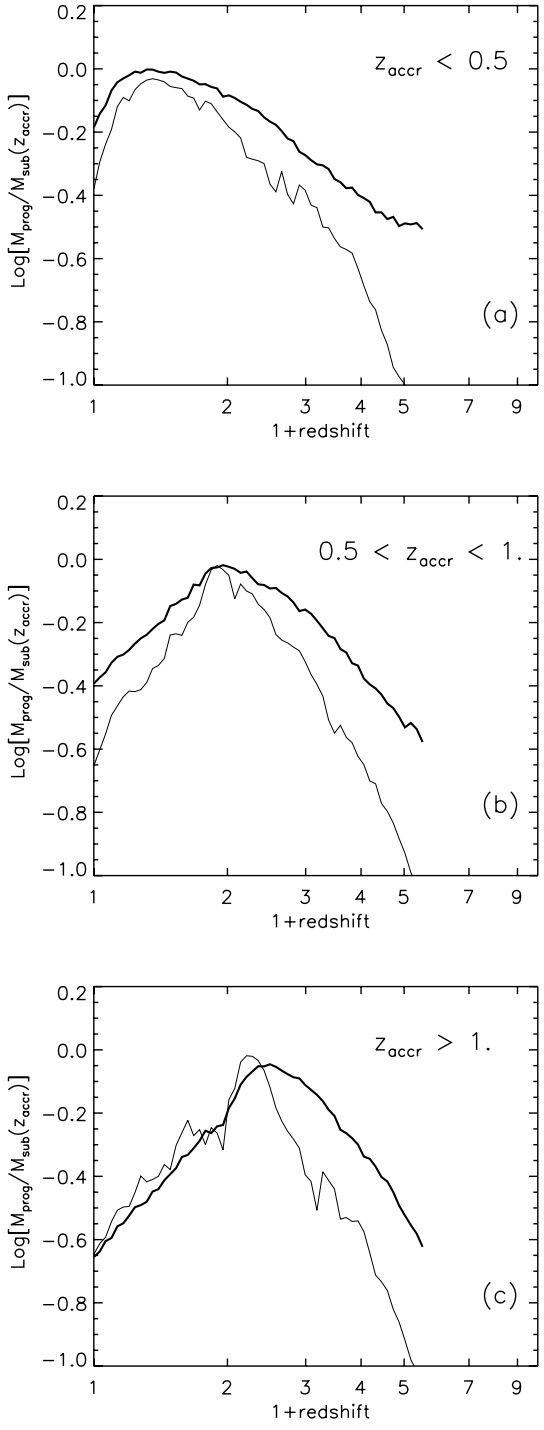

Figure 12. Average mass accretion history for $z = 0$ cluster subhaloes accreted in three different redshift bins. Thick lines are used for subhaloes with mass $\sim 10^{11}\ h^{-1}\ {\rm M}_\odot$ and thin lines are used for subhaloes with mass $\sim 10^{12}\ h^{-1}\ {\rm M}_\odot$. The histories are normalized to the mass of the subhalo at the accretion time.

checking as substructures are accreted on to the main progenitor. We count as mergers all accretion events involving haloes with mass larger than $2 \times 10^{10}\ h^{-1}\ {\rm M}_\odot$ and mass ratio smaller than 5 : 1. Note that the lower limit on the mass of the merging haloes corresponds to the resolution limit of our cluster simulations (see Table 1).

In order to have enough information without running into numerical resolution effects, we limit the present analysis to subhaloes with

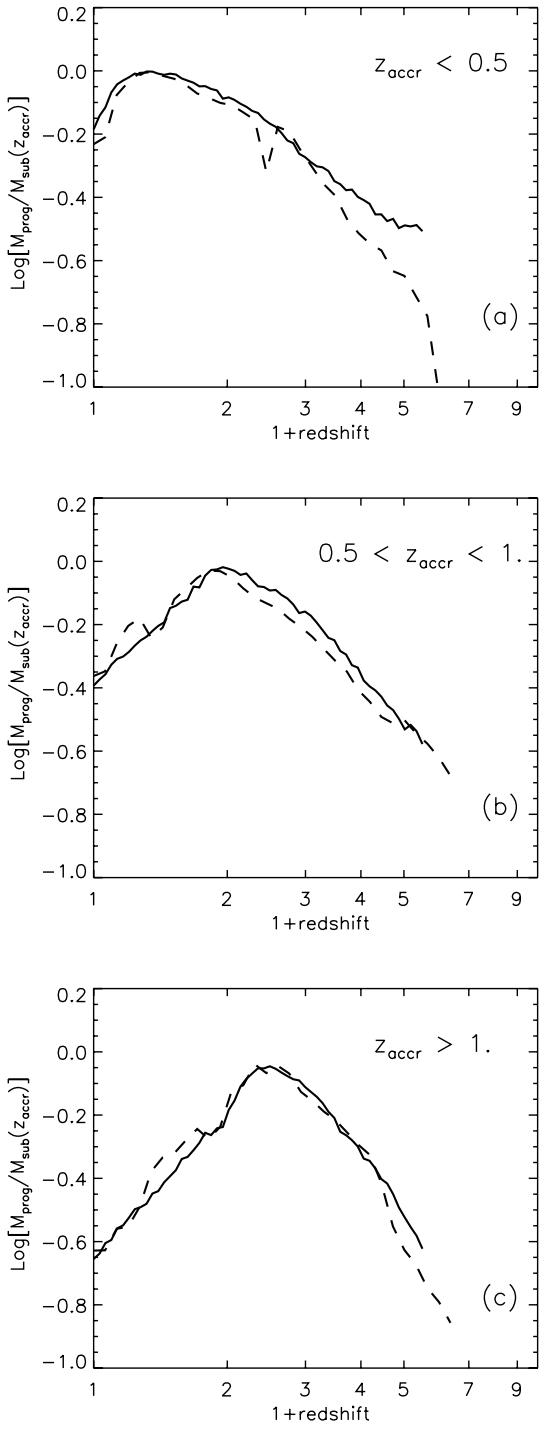

Figure 13. Mass accretion histories for our lowest-mass bin ($\sim 10^{11}\ h^{-1}$ $M_\odot$) for cluster subhaloes (solid line) and for field subhaloes (dashed line). As in Fig. 12, the sample is divided into three different subsamples according to the redshift of accretion.

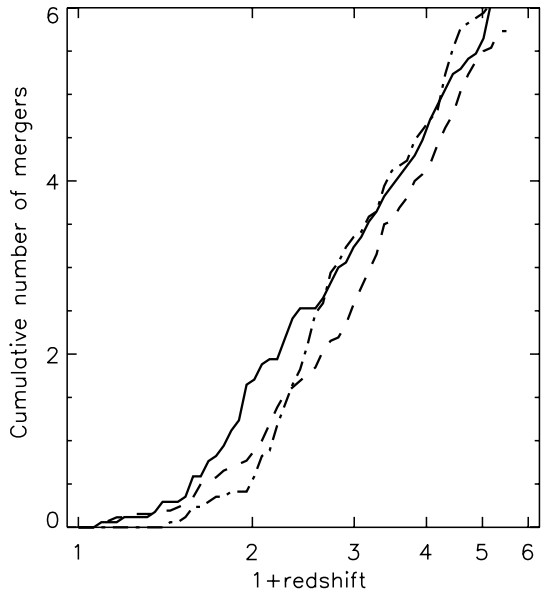

Figure 14. The mean number of mergers after redshift z for substructures selected from the simulations B1 and B2 at redshift $z = 0$ and with mass $\sim 10^{12}\ h^{-1}\ M_\odot$. The solid line is for substructures accreted at redshift $z < 0.5$, the dashed line for substructures accreted at redshift $0.5 < z < 1.0$ and the dashed-dotted line for substructures accreted at redshift $z > 1.0$.

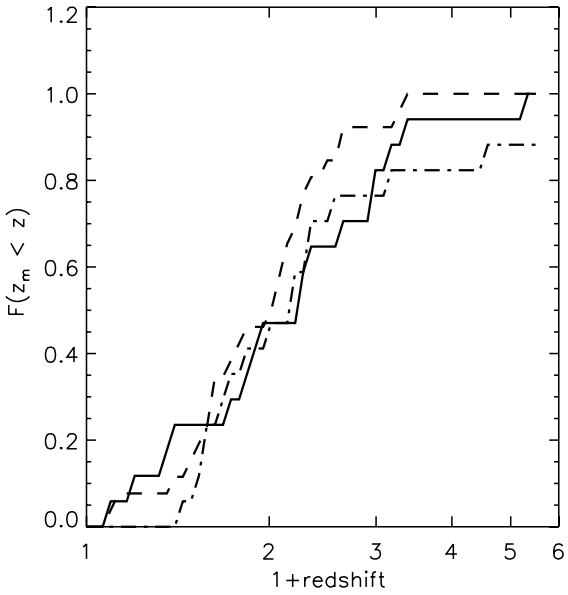

Figure 15. Fraction of substructures with at least one merger event at redshift $z_m < z$. Different line styles are for different accretion redshift as in Fig. 14.

mass $\sim 10^{12}\ h^{-1}\ M_\odot$. Fig. 14 shows the mean number of mergers per subhalo, identified at redshift $z = 0$, occurring after the redshift plotted in the abscissa. As in the previous section, the sample is split into three different accretion redshift intervals.

Merger events are less frequent once a halo is accreted on to a more massive structure. This is because the merging efficiency is higher in environments where the relative velocities of subhaloes are similar to their internal virial velocities. Once haloes are accreted by a massive halo, merging is suppressed by the large velocity dispersion they aquire. This effect is clearly visible in Fig. 14 in the change in slope of the curves near the accretion redshift. Note, however, that when one goes to significantly higher redshift the difference between the three curves vanishes.

In Fig. 15 we show the fraction of subhaloes that have had at least one merger after the redshift plotted in the abscissa. Note that the merger events we are considering are characterized by similar masses and will most likely influence the morphology of the main

galaxy, leading to the formation of a bulge component. The final morphology of the galaxies residing in these substructures will depend on the time between the last major merger and accretion on to the cluster: the longer this time, the larger is the likelihood that the galaxy can grow a new disc.

The results in Fig. 15 show that ∼80 per cent of the $\sim 10^{12}\ h^{-1}$ $M_\odot$ haloes in our $z = 0$ sample have had at least one major merger at redshift below *2*; this fraction decreases to ∼ 40 per cent for redshift <1. Surprisingly the fraction is almost independent of the accretion time. These results suggest that a large fraction of subhaloes in our cluster sample will host early-type galaxies with a significant bulge component.

8 SUMMARY AND DISCUSSION

We have used a set of high-resolution numerical simulations in a ΛCDM universe to study dark matter halo substructures. Such dark matter substructures mark the sites where luminous galaxies are expected to be found, so the analysis of their mass functions, radial distributions, merging and mass accretion histories should help us to understand better the properties of the galaxies that form in hierarchical galaxy formation models. Comparison with observational data should then suggest the physics that needs to be included in viable models of galaxy formation and evolution.

In agreement with previous work (Moore et al. 1999b), we find that the shape of the subhalo mass function is almost independent of the mass of the parent halo, with galactic haloes being essentially scaled versions of cluster haloes.

We find that the average mass of the largest substructure within the virial radius (excluding the BCG) scales linearly with the mass of the parent halo. If the stellar masses scale linearly with the dark matter mass of the parent substructure, the second-ranked galaxies should have *K*-band luminosities that increase roughly linearly with the mass of the main halo and are equal to those of the third-ranked galaxies to within 0.5 mag.

Note that the assumption that the stellar mass scales linearly with the dark matter mass of the parent substructure cannot generally be true since stars are typically much more concentrated than dark matter. The relation between stellar mass and the mass of parent substructure is then quite complex and should be followed considering the details of star formation and feedback process as is done for example in Springel et al. (2001b).

We have also used the simulations to study the radial distribution of substructures. In agreement with previous work (Ghigna et al. 2000), we find that the radial profile of substructure number density is 'antibiased' relative to the dark matter profile in the inner regions of haloes. The most massive substructures reside preferentially in the outer regions of haloes. This is, at least in part, because substructures undergo substantial tidal stripping in the dense inner regions of haloes.

We have studied the evolution with time of this stripping process and find that once a subhalo is accreted by a larger system, tidal stripping is highly effective; the longer a substructure spends in a more massive halo, the larger is the destructive effect. This suggests that substructures are constantly erased in clusters, being replenished by newly infalling galaxies.

Interestingly, a significant fraction of the substructures found in present-day clusters were first accreted at redshifts $z < 1$, implying that tidal truncation of the dark haloes of cluster galaxies happened relatively recently, and that at $z > 1$ many present-day 'passive' cluster members should still have been central galaxies of their own extended dark haloes. If gas was able to cool in these haloes, the galaxies may have been considerably more active at $z \sim 1$ than at present. Substructures in smaller haloes have histories remarkably similar to those in cluster haloes, suggesting that the efficiency of tidal stripping is largely independent of the mass of the main halo.

Once a substructure is accreted on to a cluster, its merging probability decreases because of the large velocity dispersion of the system. Observational data are currently being collected on merger rates in different environments (Patton et al. 1997; van Dokkum et al. 1999). In future work, we plan to carry out a more direct comparison with observational data of this kind, and so to test the hierarchical paradigm for galaxy formation in new ways.

ACKNOWLEDGMENTS

The simulations presented in this paper were carried out on the T3E supercomputer at the Computing Centre of the Max-Planck-Society in Garching, Germany and on the IBM SP2 at CINES in Montpellier, France.

We thank Antonaldo Diaferio, Gao Liang and the referee, Fabio Governato, for useful comments and discussions that significantly improved the presentation.

GDL thanks the Alexander von Humboldt Foundation, the Federal Ministry of Education and Research, and the Programme for Investment in the Future (ZIP) of the German Government for financial support.

REFERENCES

Barnes J. E., 1999, in Beckman J. E., Mahoney T. J., eds, ASP Conf. Ser. Vol. 187, Evolution of Galaxies on Cosmological Time-Scales. Astron. Soc. Pac., San Francisco, p. 293
Benson A. J., Frenk C. S., Lacey C. G., Baugh C. M., Cole S., 2002, MNRAS, 333, 177
Bond J. R., Cole S., Efstathiou G., Kaiser N., 1991, ApJ, 379, 440
van den Bosch F., 2002, MNRAS, 331, 98
Bower R., 1991, MNRAS, 248, 332
Bullock J. S., Kravtsov A. V., Weinberg D. H., 2000, ApJ, 539, 517
Chiba M., 2002, ApJ, 565, 17
Colin P., Avila-Reese V., Valenzuela O., Firmani C., 2002, ApJ, 581, 777
Dalal N., Kochanek C., 2002, ApJ, 572, 25
van Dokkum P. G., Franx M., Fabricant D., Kelson D. D., Illingworth G., 1999, AJ, 520, L95
Efstathiou G., 1992, MNRAS, 256, 43
Ghigna S., Moore B., Governato F., Lake G., Quinn T., Stadel J., 1998, MNRAS, 300, 146
Ghigna S., Moore B., Governato F., Lake G., Quinn T., Stadel J., 2000, ApJ, 544, 616
Gottlöber S., Klypin A. A., Kravtsov A. V., 1999, in Banday A. J., Sheth R. K., da Costa L. N., eds, Evolution of Large-Scale Structure: From Recombination to Garching. European Southern Obser., Garching, p. 358
Helmi A., White S. D. M., Springel V., 2002, Phys. Rev. D, 66, 063502
Jenkins A., Frenk C. S., White S. D. M., Colberg J. M., Cole S., Evrard A. E., Couchman H. M. P., Yoshida N., 2001, MNRAS, 321, 372
Lanzoni B., Cappi A., Ciotti L., Tormen G., Zamorani G., 2003, ApJ, in press (astro-ph/0307141)
Macfarland T., Couchman H. M. P., Pearce F. R., Pichlmeier J., 1998, New Astron., 3, 687
Mao S., Schneider P., 1998, MNRAS, 295, 587
Moore B., Katz N., Lake G., 1996, ApJ, 457, 455
Moore B., Quinn T., Governato F., Stadel J., Lake G., 1999a, MNRAS, 310, 1147
Moore B., Ghigna S., Governato F., Lake G., Quinn T., Stadel J., Tozzi P., 1999b, ApJ, 524, L19
Katz N., White S. D. M., 1993, ApJ, 412, 455
Kauffmann G., White S. D. M., Guiderdoni B., 1993, MNRAS, 264, 201

Kauffmann G., Colberg J. M., Diaferio A., White S. D. M., 1999, MNRAS, 303, 188
Klypin A., Gottlober S., Kravstov A. V., Khokhlov A. M., 1999a, ApJ, 516, 530
Klypin A., Kravstov A. V., Valenzuela O., Prada F., 1999b, ApJ, 522, 82
Patton D. R., Pritchet C. J., Yee H. K. C., Ellingson E., Carlberg R. G., 1997, ApJ, 475, 29
Power C., Navarro J. F., Jenkins A., Frenk C. S., White S. D. M., Springel V., Stadel J., Quinn T., 2003, MNRAS, 338, 14
Press W., Shechter P., 1974, ApJ, 187, 425
Schweizer F., Seitzer P., 1992, AJ, 104, 1039
Sheth R. K., 2003, MNRAS, 345, 1200
Somerville R. S., 2002, ApJ, 572, L23
Springel V., Yoshida N., White S. D. M., 2001a, New Astron., 6, 79
Springel V., White S. D. M., Tormen G., Kauffmann G., 2001b, MNRAS, 328, 726
Stoehr F., White S. D. M., Tormen G., Springel V., 2002, MNRAS, 335, L84
Stoehr F., White S. D. M., Springel V., Tormen G., Yoshida N., 2003, ApJ, in press (astro-ph/0307026)
Stoehr F., PhD thesis, 2003, Ludwig Maximilian Univ. München
Tasitsiomi A., 2002, preprint (astro-ph/0205464)
Tormen G., Bouchet F. R., White S. D. M., 1997, MNRAS, 286, 865
Tormen G., Diaferio A., Syer D., 1998, MNRAS, 299, 728
Whitmore B. C., Miller B. W., Schweizer F., Fall S. M., 1997, AJ, 114, 1797
Yoshida N., Sheth R. K., Diaferio A., 2001, MNRAS, 328, 669

This paper has been typeset from a TEX/LATEX file prepared by the author.